Available online at www.sciencedirect.com

jmr&t
Journal of Materials Research and Technology

journal homepage: www.elsevier.com/locate/jmrt

Original Article

Constitutive modeling and hot deformation processing map of a new biomaterial Ti–14Cr alloy

Sumit Ghosh [a], Atef Hamada [b,*], Madan Patnamsetty [c], Wojciech Borek [d], Mohammed Gouda [e], Akihiko Chiba [f], Saad Ebied [g]

[a] Materials and Mechanical Engineering, Centre for Advanced Steels Research, University of Oulu, FI-90014, Finland
[b] Kerttu Saalasti Institute, Future Manufacturing Technologies (FMT) Unit, University of Oulu, Pajatie 5, 85500 Nivala, Finland
[c] Materials Science and Environmental Engineering, Tampere University, 33720, Tampere, Finland
[d] Institute of Engineering Materials and Biomaterials, Silesian University of Technology, Ul. Konarskiego 18a, 44-100 Gliwice, Poland
[e] Mining and Petroleum Engineering Department Al-Azhar University Al Nasr Road, Nasr City, 11751, Cairo, Egypt
[f] Institute for Materials Research, Tohoku University, 2-1-1 Katahira, Aoba-ku, Sendai, 980-8577, Japan
[g] Department of Production Engineering and Mechanical Design, Faculty of Engineering, Tanta University, Tanta, 31527, Egypt

ARTICLE INFO

Article history:
Received 13 July 2022
Accepted 29 August 2022
Available online 6 September 2022

Keywords:
Beta (β)-Titanium alloys
Hot deformation
Softening mechanism
Flow stress model
Processing map

ABSTRACT

A new biomaterial Ti–14Cr alloy was designed for biomedical applications. The manufacturing process of Ti alloys through hot deformation is crucial for controlling the grain structure and the mechanical performance of the alloy. In the present study, several compression tests at elevated temperatures (1123–1273 K) and strain rate ranges of 0.01 –10 s^{-1} were conducted using a Gleeble-3800 thermomechanical simulator. A processing map of the studied alloy was constructed using the principles of the dynamic material model to evaluate the hot workability and deformation mechanisms at different ranges of temperature and strain rate. The resulting grain structure was correlated with the processing map.

The processing map showed that adiabatic shear bands are expected to form at low temperatures (1123–1223 K) and moderate to high strain rates (1–10 s^{-1}), whereas the nucleation of wedge cracks is likely to develop at the grain boundary at high temperatures and low strain rates (1248–1273/0.01 s^{-1}). Consequently, a deterministic domain in the temperature and strain rate ranges of 1148–1273 K and 0.01–0.1 s^{-1}, respectively, was identified as the domain of dynamic recrystallization with a peak efficiency of the order of ~70% at 1173 K/0.01 s^{-1}, and these were considered to be the optimum parameters for hot deformation. The constitutive flow behavior was modeled based on the hyperbolic –sinusoidal Arrhenius-type equations, and a mathematical relation was used to elucidate the influence of true strain on material constants.

* Corresponding author.
E-mail addresses: atef.hamadasaleh@oulu.fi, atef.hamada@gmail.com (A. Hamada).
https://doi.org/10.1016/j.jmrt.2022.08.160

1. Introduction

People worldwide wish for a good lifestyle and better healthcare. Inevitably, people struggle to maintain the quality of healthcare with an increasing age owing to age-related health issues. Moreover, the aging population has been increasing considerably. In 2019, as reported by the United Nations, approximately 16.67% of the world population will be over the age of 65 by 2050, a significant increase from 9% in 2019 [1]. As a result, new biomaterials are needed to replace, restore, or regenerate bone, and this has caused a major concern for clinical necessity in dental, spinal fixation, orthopedic, cranial, and maxillofacial surgery [2].

Titanium and its alloys have been used in several biomedical applications owing to their acceptable mechanical properties, excellent resistance to corrosive environments, and high biocompatibility [3,4]. For instance, the most extensively used Ti alloy in many biomedical applications is Ti64 (Ti–6Al–4V), which has a typical two-phase structure (α+β-type) and a high Young's modulus (~110 GPa), approximately half that of SUS 316L stainless steel (~200 GPa) [5–7]. However, owing to the toxicity of vanadium and higher Young's modulus than that of bone (~10–30 GPa), this alloy is not suitable for bio-implants [4]. Another example of a titanium alloy used in different biomedical applications is the Ti–15Mo–5Zr–3Al alloy, which has a β-type phase structure. This alloy has high strength (<1400 MPa) with an acceptable level of ductility [8] and low elastic modulus (~44 GPa) [9]. However, Al ion release has potential neurological impacts that cause Alzheimer's disease [10]. Therefore, scientists need to produce Ti alloys free of Al and V [11,12]. Ti-2448 alloy (i.e., Ti–24Nb–4Zr–7.9Sn) is one interesting variant of Ti alloy for potential biomedical application that consists of non-toxic alloying elements (Nb, Zr, Sn). Although this alloy exhibit high strength level together with low elastic modulus. But previous studies shown a peculiar nonlinear elastic behavior of these alloys due to complex combination of various deformation mechanisms [13]. Modern α+β dual-phase Ti-xNb-yTa-2Zr alloy design approach drew significant research interest because of superior combination of lower modulus and higher plasticity. However, a series of investigation still needed to optimize the concentration level of Nb, Ta and Zr for better property [14].

Recently, Ti–Cr binary alloys have attracted considerable research attention owing to their high wear resistance, excellent strength at elevated temperatures, better oxidation resistance, and biocompatibility [15,16]. Zhao et al. [3] studied the biocompatibility and mechanical properties of a binary Ti–Cr system and found that the addition of Cr up to 14 wt.% imparts high strength and high biocompatibility compared with SUS 316L. In addition, they showed that the tensile strengths of all the studied alloys exposed to solution treatment were higher than 700 MPa [17]. Cr has the ability to manipulate the anodic activity of the alloy and raise the tendency of Ti to passivate [18], and this passive film formation on Ti alloys, sequentially, increases resistance to corrosion [19–21]. Hanada and Izum [22] investigated the cold deformability of binary Ti–Cr alloys. They showed that slip occurs through the deformation of alloys containing a high chromium fraction and twins in alloys with lower β-phase stability [22]. Ho et al. [23] elucidated that Ti–20Cr is the most suitable alloy for applications in prosthetic dentistry because it introduces other dental casting properties.

Hot deformation is a vital and significant step in the manufacturing of metallic materials, and several studies have been conducted on this subject. For the majority of metallic alloys, the glide and slip of dislocations are vital plastic working modes, such as in titanium alloys [1–4], steel alloys [2–31], and high-entropy alloys [32–34]. In addition to the dislocation motion, other essential deformation modes, such as twinning, dynamic recrystallization (DRX), and phase transformation, have been observed in several metals. Among metallic alloys, β-Ti alloys have specific importance for many applications, such as aerospace structural applications and biomedical and chemical industries, because of their high strength-to-density ratio and outstanding corrosion resistance [35,36].

Thermomechanical processing is considered a basis for controlling the mechanical properties of titanium alloys [37,38]. In thermomechanical processing, hot deformation plays a significant role, which is related to microstructure control [39]. For β-Ti alloys, the microstructure is sensitive to the factors of the hot forming process, and frequent attentiveness is required to comprehend the impacts of the processing parameters on the deformed microstructure characteristics of β-Ti alloys, specifically monitoring the processing parameters and achieving an ideal microstructure and optimal mechanical properties. Physical thermal simulations and processing maps are beneficial techniques for characterizing the behavior of materials through hot deformation [40–42].

For β-Ti alloys, in the β-phase region, dynamic recovery (DRV) is the prime controlling deformation mechanism for microstructure evaluation through hot forming. However, in previous studies, DRX of the beta phase has been proven in several alloys [43–45]. Although this is important from both industrial and scientific viewpoints, no robust proof is available for the trace of deformation variables on DRX as a deformation mechanism in different β-Ti alloys [46]. Matsumoto et al. [47] studied the hot forming behavior of the Ti–5Al–5V–5Mo–3Cr alloy in the single β-phase region and built its processing map at forming temperatures in the range of 1123–1273 K. They concluded that the DRV-dominated softening mechanism was changed to DRX -dominated deformation when the deformation temperature was higher than 1123 K and flow instability occurred at a high strain of over 0.05 s^{-1}. Furthermore, in our previous study, the microstructure investigation of the Ti–14Mn alloy revealed that DRV was more active than DRX throughout the deformation temperature range [24]. Liu et al. [48] studied the hot formability of near-β Ti–5Al–5Mo–5V–1Cr–1Fe alloy. They deduced that DRV was the controlling deformation mechanism within a single β-phase region. However, a continuous dynamic recrystallization (CDRX) mechanism has not been proven to be responsible for comprehensive grain refining and excellent workability in β-Ti alloys [49]. Although

the idea of CDRX in β-Ti alloys has been suggested by some researchers [50], other researchers have considered conventional discontinuous DRX (DDRX) [46]. Recently, Li et al. [51] investigated the hot-forming mechanism of the Ti–6Cr–5Mo–5V–4Al alloy in the single-phase region. DDRX mainly occurred in the high-temperature and low strain-rate domains, whereas the CDRX deformation mechanism occurred in the elevated strain-rate domain. Thus, additional studies are required to solve the debates regarding the dynamic softening mechanism in β-Ti alloys.

Our present study investigates the hot-deformation behavior and the corresponding deformation mechanisms during hot compression of a β Ti–14Cr alloy for biomedical applications. A series of isothermal compression tests at high temperatures were conducted using a Gleeble-3800 thermomechanical simulator. The study reveals the hot-forming behavior of the Ti–14Cr alloy is elucidated, which facilitates optimizing the manufacture of this alloy, and therefore its microstructure and mechanical properties. This goal is achieved by constructing a processing map to recognize the active deformation mechanisms. This study would enable the manufacture of low-cost Ti–14Cr alloys via optimized processing routes at high temperatures and various strain rates.

2. Experimental methods

The Ti–14 wt.% Cr alloy used in this study was designed according to the molybdenum equivalent (Mo_{eq}) of the Cr addition. The β-*bcc* phase stability in Ti-based alloys is significantly related to the Mo_{eq} [52–54] of the alloying element additions. With an increasing Mo_{eq}, the stability of the β-bcc phase increases. Ti–14Cr was prepared by melting high-purity Ti and Cr in an electric arc furnace (Model: ACM-08-1000S, Tokyo, Japan) under an argon atmosphere. The melt was subsequently cast as 200 g ingots. Subsequently, the alloy ingots were homogenized at 1373 K for 21.6 ks under a protective argon atmosphere. The alloy was hot-rolled at 1173 K using a laboratory hot-rolling mill at Tohoku University, Japan, to produce rods 10 mm in diameter. The rods were encapsulated in a quartz tube filled with argon gas and then solution heat-treated at 1173 K for 1.8 ks in a muffle furnace, followed by quenching in ice water to induce a full β-phase structure at room temperature, *see* Fig. 1.

Specimens of dimensions ~φ 8 mm × 12 mm with an aspect ratio of 1.5 were extracted from the solution-treated material rods using the machining process.

High-temperature compression tests were conducted using a Gleeble 3800® thermomechanical simulator (Dynamic Systems Inc., Poestenkill, NY, USA). The applied hot-deformation cycle is shown in Fig. 1. The tests were performed in the temperature range of 1123–1273 K in steps of 50 K, and the strain range was varied in the range of 0.01–10 s^{-1}. After the compression tests, the specimens were cooled in compressed air. A graphite foil was employed between the cylindrical specimen and the compression anvils to minimize friction. In addition, a tantalum foil was used to prevent sticking to the anvils. The hot compression data were evaluated using the MATLAB® 2020a program, and true stress–strain plots were constructed using the Origin® 2017 software.

The microstructures of the specimens were examined using an electron back-scattered diffraction (EBSD) facility equipped with a Zeiss Sigma field-emission scanning electron microscope. The deformed specimens were sectioned at the midplane parallel to the compression axis and polished using a standard metallographic procedure. The samples were first rough-polished using abrasive SiC papers, followed by a colloidal silica suspension (0.04 μm) as the final step for polishing. The EBSD measurements of selected specimens were further processed using the CHANNEL 5 data package. Grain boundaries (GBs) were categorized as high-angle (HAGBs) and low-angle grain boundaries (LAGBs), corresponding to misorientation angle (φ) ranges of $\geq 15^{\circ}$ and $2^{\circ} < \varphi < 15^{\circ}$, respectively, to determine the microstructure characteristics. The crystallographic structures of the hot-rolled samples were examined by X-ray diffraction (XRD) using a Rigaku SmartLab XRD diffractometer operated on a Co–K_{α} radiation source.

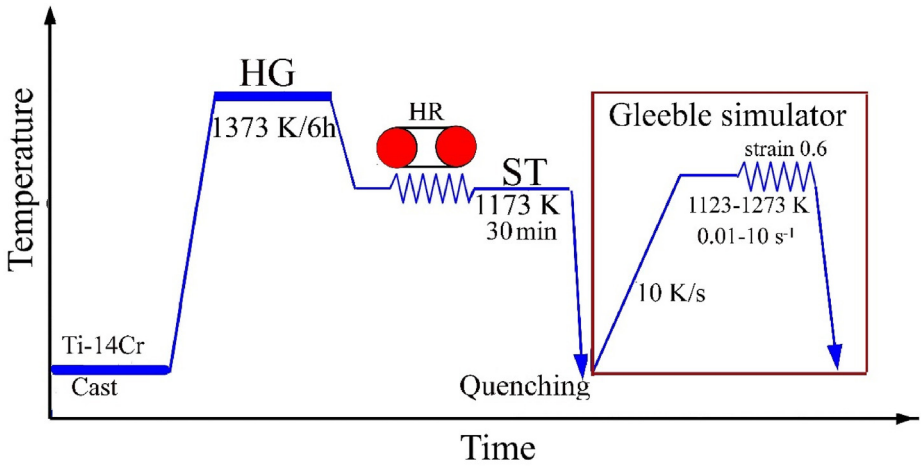

Fig. 1 – Schematic diagram showing the heating and deformation parameters during the thermo-mechanical processing of the Ti–14Cr alloy (HG: homogenization; ST: solution treatment; HR: hot-rolling).

3. Results and discussion

3.1. Initial microstructure

The typical microstructure of the solution-treated Ti–14Cr alloy at 1173 K was examined using EBSD, and the data were acquired in the plane normal to the rolling direction (i.e., parallel to the compression axis of the test samples). The microstructure, as shown in Fig. 2, comprised equiaxed grains with an average grain size of ~150 μm. Fig. 2(a) shows the image quality (IQ) map of the microstructure of the studied Ti–14Cr alloy. Coarse grains of the β-bcc matrix were observed without the precipitation of a secondary phase, such as Laves phase ($TiCr_2$) which exists in the Ti–Cr phase diagram [55]. This indicates that 14 wt.% Cr stabilizes the β-phase at room temperature. The orientation map of the initial grain structure, that is, the inverse pole figure (IPF), exhibits a random crystallographic orientation for the grains because different colors of the grain orientations are displayed, as shown in Fig. 2(b). The XRD pattern was analyzed to identify the phases present in the solution-treated microstructure. The peaks in the XRD pattern of the Ti–14Cr alloy were indexed to the β-*bcc* structure, as shown in Fig. 2(c).

3.2. Flow stress behavior

Fig. 3(a–d) show typical true stress–strain curves of the Ti–14Cr alloy plotted from the hot compression data in the temperature and strain rate ranges of 1123–1273 K and 0.01–10 s^{-1}, respectively. Fig. 3 depicts a change in flow stress behavior with respect to strain rate and/or deformation temperature. Irrespective of the strain rate, at initial strains, the flow stress increased with increasing true strain under all test conditions due to work hardening. Application of initial strains leads to the enhancement of dislocation density with subgrain formation. In general, the work hardening rate and peak stress expectedly increased with a decrease in temperature and increase in strain rate, i.e., with an increasing Zener–Hollomon parameter (Z) [56].

A characteristic peak stress behavior is observed in the flow stress at all test temperatures and low strain rates of 0.01 and 0.1 s^{-1}, followed by flow softening upon further straining. The continuous flow softening can be recognized as DRX due to microstructural reconstitution or localized/unstable plastic flow. The DRX phenomenon is generally observed during the high-temperature compression of FCC-based alloys with low or intermediate stacking fault energies (SFE) [57–59]. Mainly at higher temperatures (1223–1273 K) and lower strain rates (0.01–0.1 s^{-1}), typical peak stress and flow softening behavior followed by steady-state was achieved in the flow stress curves, suggesting that the DRX process was complete, and grain growth occurred. At a low strain rate (0.01 s^{-1}) and low temperatures, mainly at 1123 K, features typical for softening may be attributed to flow localization [60]. However, with a further increase in the strain rate, the flow localization gradually disappeared as the flow stress behavior attained steadiness,

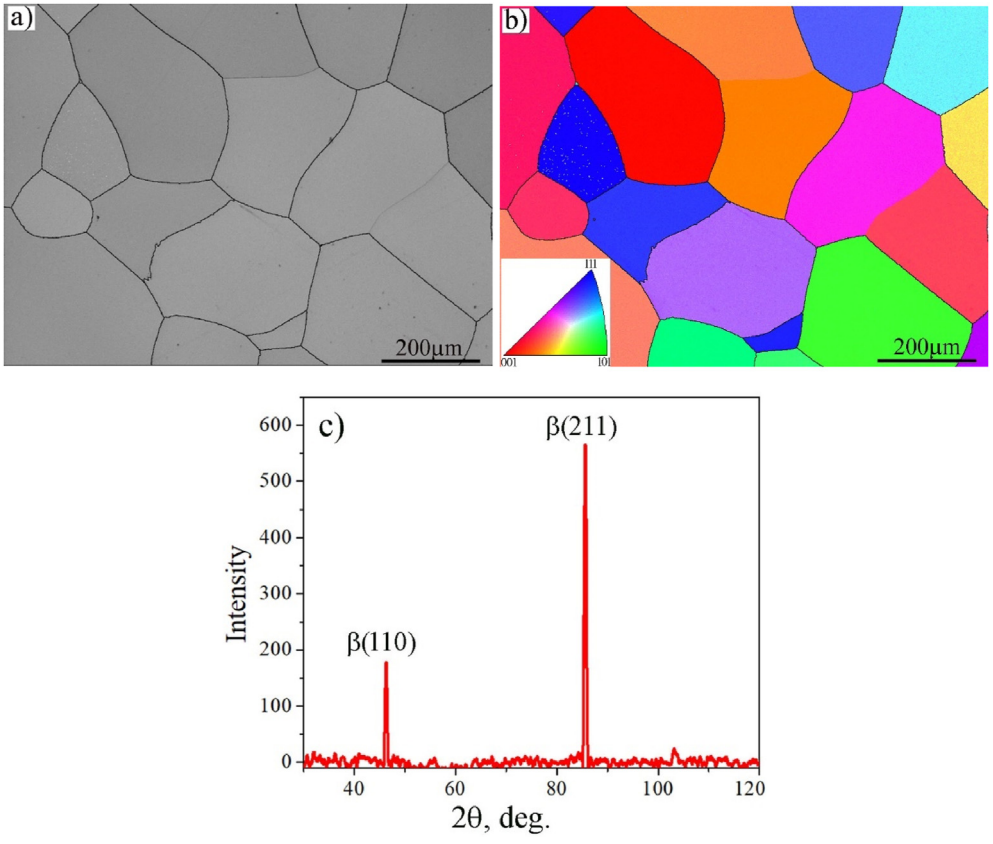

Fig. 2 – EBSD maps of the microstructure of the Ti–14Cr solution treated at 1173 K for 1.8 ks. (a) IQ map, (b) EBSD orientation map, and (c) XRD pattern of the corresponding microstructure in (a).

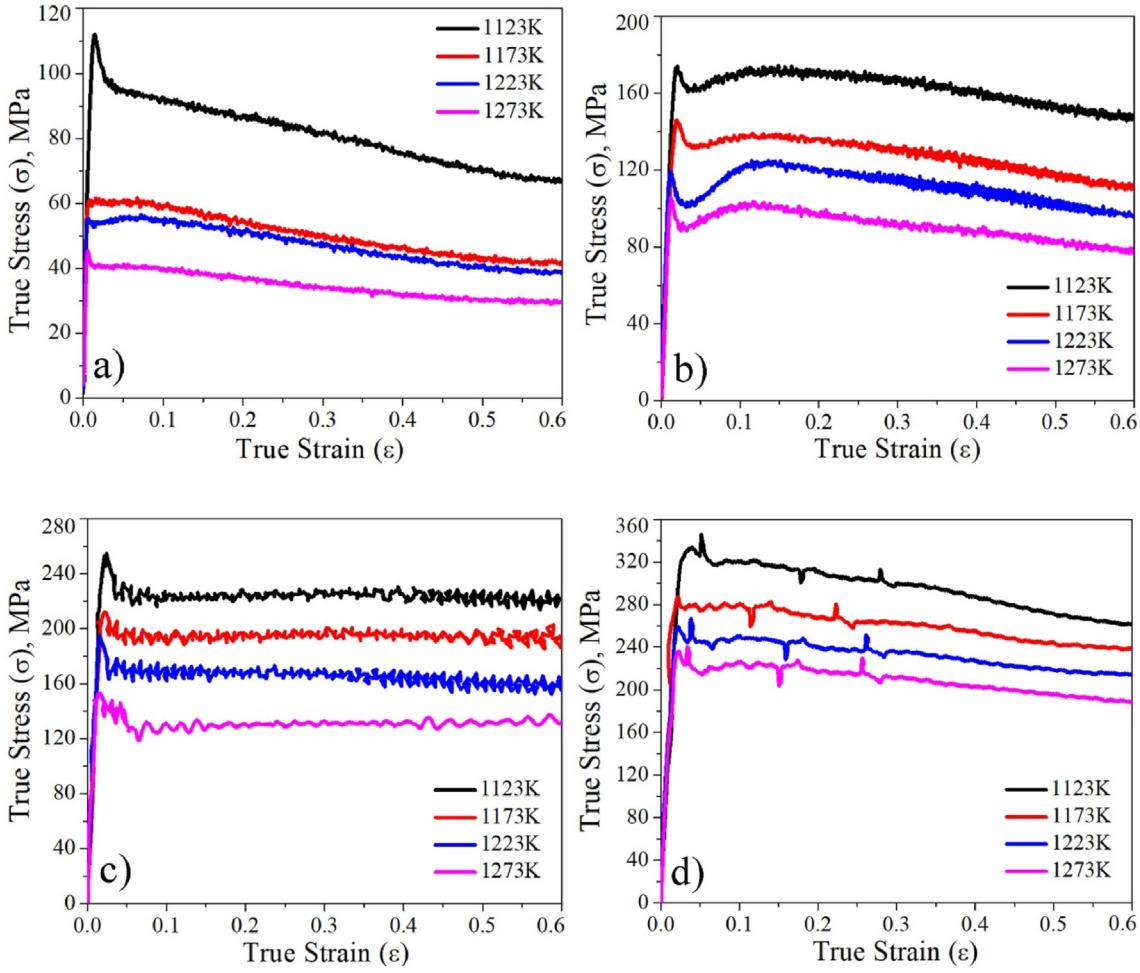

Fig. 3 – True stress–strain curves at different temperatures and strain rates: (a) at 0.01 s^{-1}, (b) at 0.1 s^{-1}, (c) at 1 s^{-1}, (d) at 10 s^{-1}.

which is typical for dynamic recovery (DRV). The operating softening mechanism during the hot deformation of the concerned alloy was determined by the observation of microstructure using the EBSD, shown in Section 3.6.

It should be noted that at 1 s^{-1}, the flow curves are almost approaching a steady state. The steady-state flow is reminiscent of a dynamic balance between strain hardening and flow softening due to dynamic recovery. However, at 10 s^{-1} the flow softening behavior is observed which may be due to the adiabatic heating. In agreement, Hamada et al. [61] reported that at a high strain rate of 10 s^{-1}, an adiabatic temperature rise is promoted during the hot deformation process. Consequently, the flow stress curves decrease at the high strain rate of 10 s^{-1}, especially at low temperatures.

3.3. *Arrhenius-type constitutive equation*

A hyperbolic sinusoidal Arrhenius-type equation incorporating the activation energy of deformation (Q_{def}) was used to define the constitutive relationship between the strain rate, flow stress, and deformation temperature [62]. The Zener–Holloman parameter (Z), often referred to as the temperature-compensated strain rate, is typically used for the simultaneous analysis of the strain rate and temperature dependence of plastic deformation. The corresponding set of equations is especially applicable for hot deformation because the high-temperature flow behavior of the deforming alloy is controlled by thermal activation [63]. Therefore, the constitutive equation is expressed as [64,65]:

$$Z = A \cdot [\sinh(\alpha\sigma)]^n = \dot{\varepsilon} \cdot \exp\left(Q_{def} \Big/ RT\right) \quad (1)$$

The Eq. (1) can be rewritten as:

$$\dot{\varepsilon} = A \cdot [\sinh(\alpha\sigma)]^n \cdot \exp\left(-Q_{def} \Big/ RT\right) \quad (2)$$

where A, α, and n are material constants independent of temperature, T is the temperature in Kelvin, R is the universal gas constant (8.314 J/(mol·K)), Q_{def} is the activation energy of deformation (J/mol), σ is the flow stress (MPa), and $\dot{\varepsilon}$ is the strain rate (s^{-1}). Equation (2) can be expressed in three different forms based on the stress ranges [24].

$$\dot{\varepsilon} = A_1 \cdot \sigma^{n'} \cdot \exp\left(-Q_{def} \Big/ RT\right) \quad \alpha\sigma < 0.8 \quad (\text{for low stresses}) \quad (3)$$

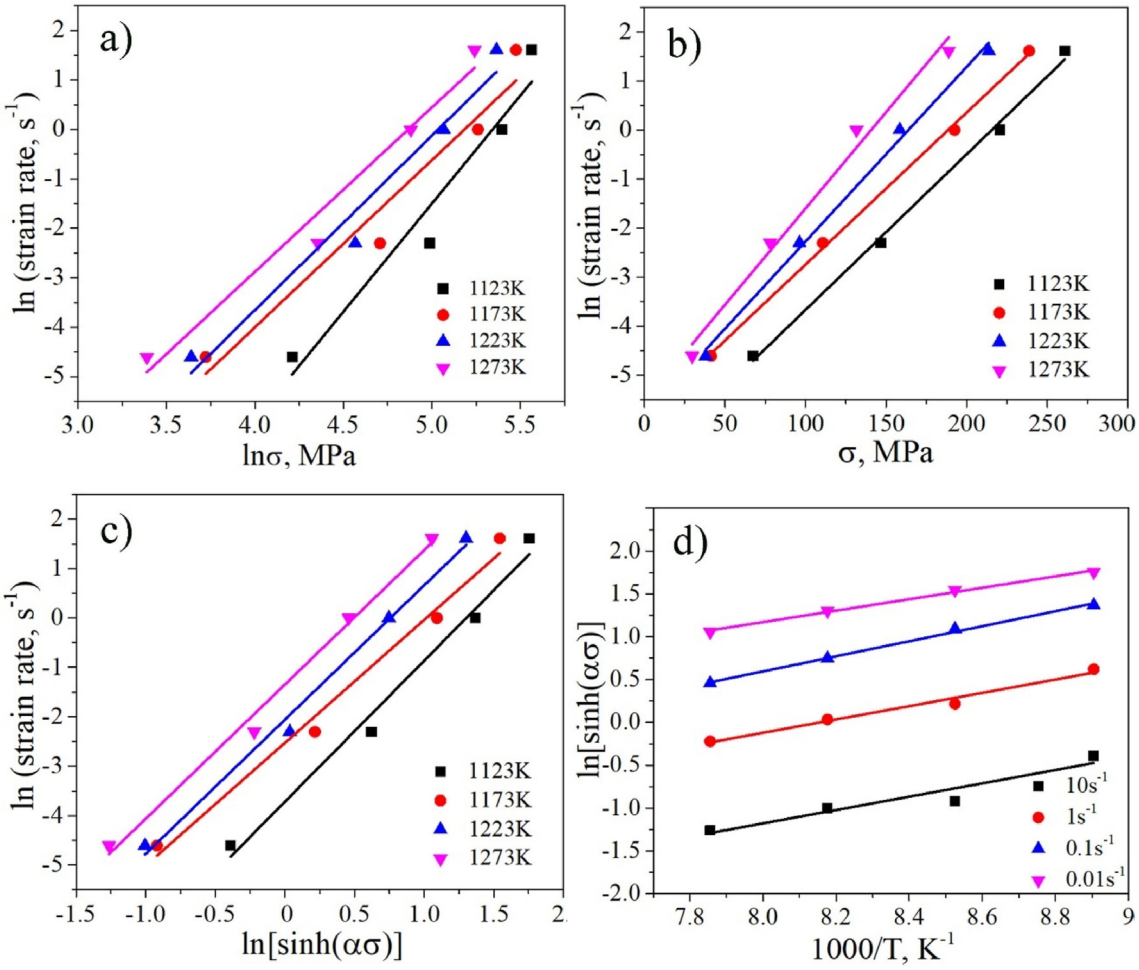

Fig. 4 – Plots of (a) $ln\dot{\varepsilon}$ vs $ln\sigma$; (b) $ln\dot{\varepsilon}$ vs σ; (c) $ln\dot{\varepsilon}$ vs $ln[sinh(\alpha\sigma)]$; and (d) $10,000/T$ vs $ln[sinh(\alpha\sigma)]$, used to estimate the material constants n', β, n, and Q_{def} values.

$$\dot{\varepsilon} = A_2 \cdot \exp(\beta\sigma) \cdot \exp\left(-Q_{def} \Big/ (RT)\right) \quad \alpha\sigma > 1.2 \quad \text{(for high stresses)} \tag{4}$$

$$\dot{\varepsilon} = A \cdot [\sinh(\alpha\sigma)]^n \cdot \exp\left(-Q_{def} \Big/ (RT)\right) \quad \text{for all } \alpha\sigma. \quad \text{(for all stresses)} \tag{5}$$

The material constants n' and β are evaluated using Eqs. (3) and (4), respectively: Accordingly, n' and β were estimated as the mean values of the slopes obtained from the linear fits of $ln\dot{\varepsilon} vs ln\sigma$ and $ln\dot{\varepsilon} vs \sigma$ plots, respectively, calculated at different test temperatures, and consequently, enabled the estimation of $\alpha(\alpha = \beta/n)$. Referring to Eq. (5), the stress exponent (n) is the mean value of the slopes of the linear fits of $ln\dot{\varepsilon} vs ln[\sinh(\alpha\sigma)]$ plots at different test temperatures. The corresponding linear fits for the slopes of n', β, and n at different temperatures are shown in Fig. 4(a–c), respectively, enabling derivation of their mean values. The Q_{def} can be expressed using Eq. (6) as follows:

$$Q_{def} = 10,000 \cdot R \cdot \left[\frac{\partial ln\dot{\varepsilon}}{\partial \ln[\sinh(\alpha\sigma)]}\right]_T \cdot \left[\frac{\partial \ln[\sinh(\alpha\sigma)]}{\partial(10,000/T)}\right]_{\dot{\varepsilon}} \tag{6}$$

The term, $\frac{\partial \ln[\sinh(\alpha\sigma)]}{\partial(10,000/T)}$ in Eq. (6) at a given strain rate is given by the slope of the linear fit of $\ln[\sinh(\alpha\sigma)]$ vs. $10,000/T$, as shown in Fig. 4(d). The value of the constant lnA in Eq. (5) can then be evaluated using the intercept on the y-axis of the linear fit of $ln(Z)$ vs. $\ln[\sinh(\alpha\sigma)]$ as shown in Fig. 5. Equation (1) can be expressed as Eq. (7) by taking the natural logarithm of both sides, thereby describing the relationship between σ and Z as

$$lnZ = lnA + n \cdot \ln[\sinh(\alpha\sigma)] \tag{7}$$

Using the material constants (α, n, A) and Q_{def} in Eqs. (3)–(5) and considering Eqs. (1) and (7), the flow stress σ can be expressed as a function of Z as follows:

$$\sigma = \frac{1}{\alpha} \cdot ln\left\{\left(\frac{Z}{A}\right)^{\frac{1}{n}} + \left[\left(\frac{Z}{A}\right)^{\frac{2}{n}} + 1\right]^{1/2}\right\} \tag{8}$$

The stress exponent n varies as a function of the strain rate and temperature. To determine the value of Q_{def} at $\varepsilon = 0.6$, the value of n was considered as the mean of the slopes, as

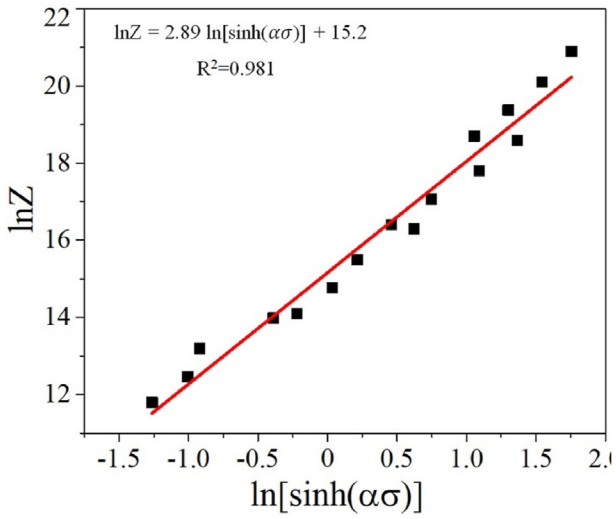

Fig. 5 – Plot of *lnZvsln*[*sinh*$(\alpha\sigma)$] to evaluate A.

shown in Fig. 4(c), at different temperatures. Accordingly, n was estimated as 2.9. From Fig. 4(d), the value of the slope was determined to be 0.77. Thus, by substituting these values into Eq. (6), the value of Q_{def} at 0.6 true strain was estimated to be approximately 182.232 kJ mol^{-1}.

A comparative analysis of the Q_{def} values with the data available in the literature for this type of titanium alloy, i.e., binary Ti-based alloys, is illustrated in Table 1.

By substituting the material constants in Eq. (8), the respective constitutive equation at $\varepsilon = 0.6$ is expressed as follows:

$$\sigma_{0.6} = \frac{1}{0.0084}\cdot ln\left\{\left(\frac{Z_{0.6}}{7\cdot 10^{11}}\right)^{\frac{1}{2.9}} + \left[\left(\frac{Z_{0.6}}{7\cdot 10^{11}}\right)^{\frac{2}{2.9}} + 1\right]^{1/2}\right\} \quad (9)$$

Where the Z at $\varepsilon = 0.6$ is expressed as:

$$Z_{0.6} = \dot{\varepsilon}\cdot \exp\left(\frac{182,232}{RT}\right) \quad (10)$$

Additionally, by substituting the material constants α, n, A, and Q_{def} in into Eq. (5), the constitutive relationship between $\dot{\varepsilon}$, T, and σ at $\varepsilon = 0.6$ can be expressed as

$$\dot{\varepsilon} = 7\cdot 10^{11}\cdot [\sinh(0.0084\cdot\sigma_{0.6})]^{2.9}\cdot \exp\,(-182,232/RT) \quad (11)$$

To define the flow stress behavior of Ti alloys at different strains over a wide strain range, the material constants α, n, Q_{def}, and A should be calculated through regression analysis considering the flow stress data at different ε values in the range of 0.1–0.6, at a step size of 0.05 strain. The relationships between the strains and the material constants were fitted using sixth-order polynomials, as shown in Fig. 6. Thus, the regression in the equations of the respective material constants α, n, A, and Q_{def} as a function of strain can be reasonably described by Eqs. (12–15), respectively:

$$\alpha = 0.0078 - 0.0228\cdot\varepsilon + 0.3043\cdot\varepsilon^2 - 1.6097\cdot\varepsilon^3 + 4,3158\cdot\varepsilon^4 - 5.6366\cdot\varepsilon^5 + 2.8393\cdot\varepsilon^6 \quad (12)$$

$$n = 3,553 - 8.9991\cdot\varepsilon + 67.344\cdot\varepsilon^2 - 262\cdot\varepsilon^3 + 493.87\cdot\varepsilon^4 - 422.94\cdot\varepsilon^5 + 123.69\cdot\varepsilon^6 \quad (13)$$

$$Q_{def} = 245.99 - 1557\cdot\varepsilon + 14785\cdot\varepsilon^2 - 65795\cdot\varepsilon^3 + 149377\cdot\varepsilon^4 - 169242\cdot\varepsilon^5 + 76136\cdot\varepsilon^6 \quad (14)$$

$$lnA = 23.058 - 160.94\cdot\varepsilon + 1489.9\cdot\varepsilon^2 - 6526.1\cdot\varepsilon^3 + 14608\cdot\varepsilon^4 - 16329\cdot\varepsilon^5 + 7254\cdot\varepsilon^6 \quad (15)$$

Table 1 – Activation energy of hot deformation Q_{def}, for some binary Ti-based alloys.

Ti alloy	Ti–14Cr present work	Ti–10Mn [24]	Ti–17Mo [53]	Ti–21Nb [66]
Q_{def} kJ/mol	182	243	283	230

3.4. *Validation of the hyperbolic–sinusoidal Arrhenius-type model*

To check the validity of the Arrhenius-type model, the predicted vs. experimental flow stress data over a broad temperature, strain, and strain rate ranges as presented in Fig. 7. The predicted flow stress values are based on Eq. (8) and Eqs. (12–15) for all strains in the range of 0.1–0.6. Fig. 7 shows that the agreement between the predicted and experimental flow stress data was satisfactory for a majority of the tests. However, the average fitting of the material constants showed significant deviations in the flow-stress data at high strain rates and low temperatures. This is because Eqs. (3) and (4) apply to low and high stress levels, respectively, and the approach used is to obtain the values of n and β using the respective equations. Therefore, these small deviations can occur depending on the accuracy of the least-squares fits and the differences in the slopes at different temperatures [67]. Such deviations ultimately affect the values of the material constants.

To assess the degree of difference between the predicted and experimental values, a standard statistical method, such as the correlation coefficient (R) and the average absolute relative error (AARE), was used as detailed in previous work [68,69]. The cumulative AARE was 9.66%, suggesting a reasonably good fit with the experimental data. The R for the least-squares fit through the experimental data was 0.9835, revealing a good relationship between the predicted flow stress and the experimental data. Fig. 8 shows the predicted flow stress curves (dashed lines) plotted in comparison with the experimental true stress–strain curves (full lines).

3.5. *Construction of processing maps based on dynamic materials model (DMM)*

The principles of dynamic material model DMM [70,71] were applied to produce a processing map to evaluate the hot-workability characteristics of Ti alloys. Accordingly, the immediate dissipation of total power (P) at any instant is majorly

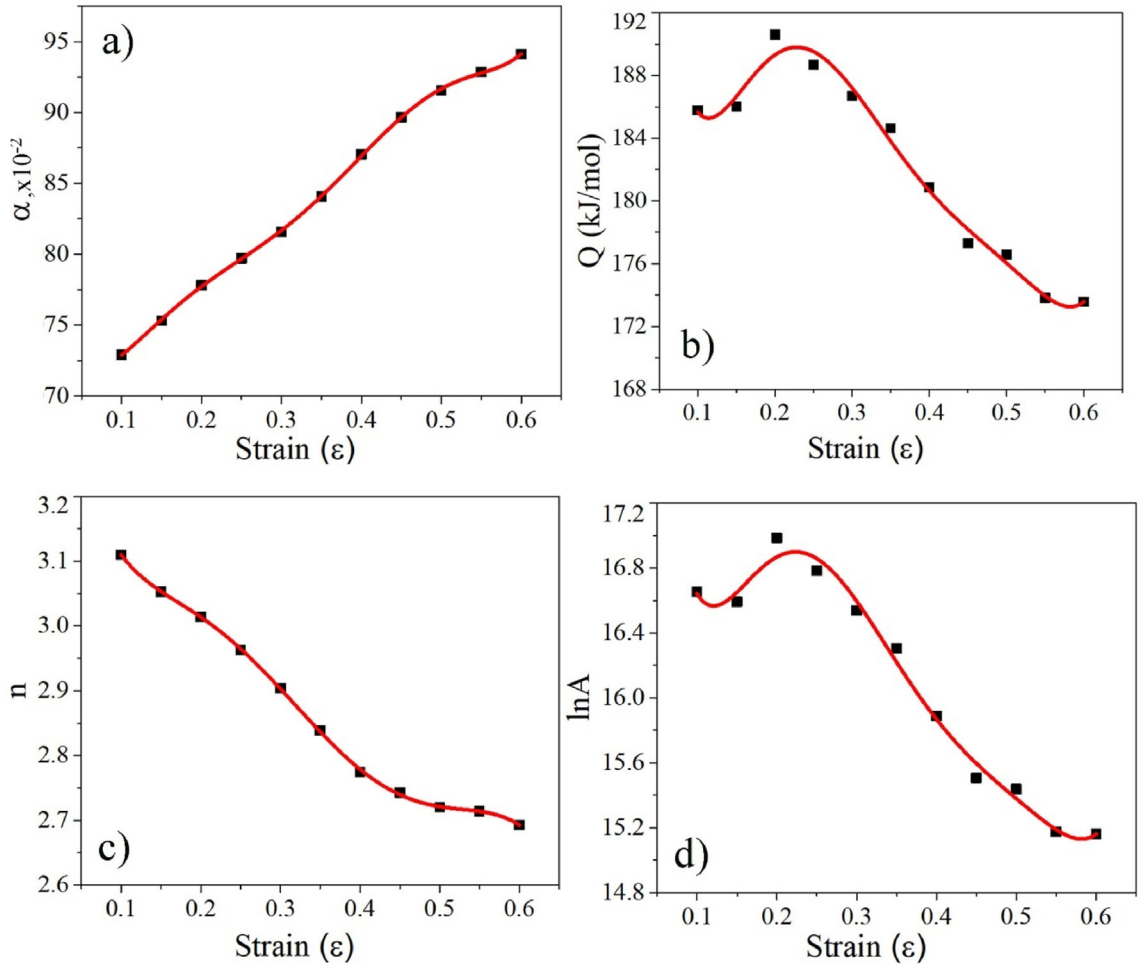

Fig. 6 – Fitting curves of the model parameters and true strain (a) α vs ε (b) Q vs ε (c) n vs ε and (d) lnA vs ε.

through a rise in temperature (*G* content) and a small fraction through changes in the microstructure (*J* co-content). The power dissipation can be expressed as:

$$P = \sigma.\dot{\varepsilon} = G + J = \int_0^{\sigma} \dot{\varepsilon} d\sigma + \int_0^{\dot{\varepsilon}} \sigma d\dot{\varepsilon} \tag{16}$$

where σ is the flow stress, $\dot{\varepsilon}$ is the strain rate, and ε is true strain. In addition, the strain rate sensitivity (m) determines the power partitioning between the *G* content and *J* co-content, and is described as follows:

$$\frac{dJ}{dG} = \frac{\dot{\varepsilon} d\sigma}{\sigma d\dot{\varepsilon}} = \frac{d(\ln\sigma)}{d(\ln\dot{\varepsilon})_{T,\varepsilon}} = m \tag{17}$$

At a given temperature and strain, *J* co–content is defined as:

$$J = \left(\sigma \cdot \dot{\varepsilon} \cdot \frac{m}{m+1}\right) \tag{18}$$

The J co-content of the workpiece, which is a non-linear dissipator, is normalised with that of an ideal linear dissipator ($m = 1$) to obtain a dimensionless parameter known as the efficiency of the power dissipation (η), expressed as

$$\eta = \frac{J}{J_{max}} = \frac{2m}{m+1} \tag{19}$$

Power dissipation efficiency describes the ability of a material to dissipate power through certain metallurgical processes; therefore, it should not be confused with the efficiency of the process. At a constant ε, the variation in η as a function of T and $\dot{\varepsilon}$ is used to establish the power dissipation map which also represents the constitutive behavior of the material [72]. A three-dimensional (3D) power dissipation map plotted as a function of T and $\dot{\varepsilon}$ could have valleys and hills depending on η values. In addition, a two-dimensional (2D) iso-efficiency contour map can be a better representation of the power dissipation map, where the centers of deterministic domains often show peak efficiency values. These deterministic domains, identified as hills in 3D power dissipation maps, are separated by bifurcation regimes (valleys) and can be construed based on their shapes and peak efficiencies and correlated with the manifestation of specific microstructural evolutions.

Prasad et al. [73] developed a continuum criterion based on the extremum principles of irreversible thermodynamics, as applied to large plastic flow described by Ziegler

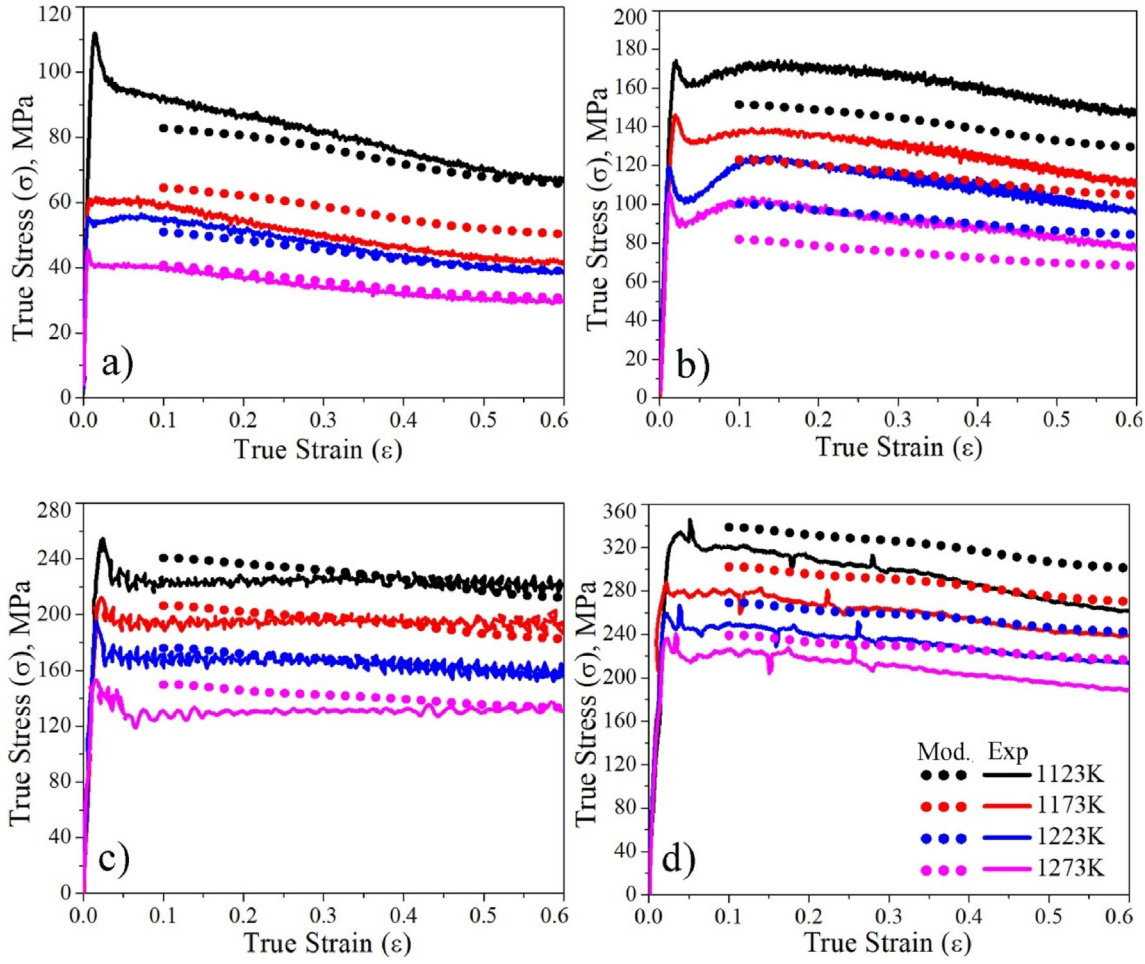

Fig. 7 – Predicted vs. Experimental flow-stress values.

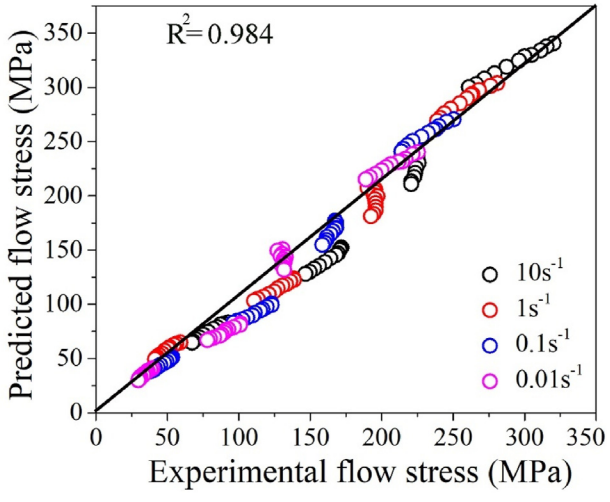

Fig. 8 – Comparison between predicted and experimental flow-stress values.

et al. [74] to identify the regimes of flow instabilities in the temperature–strain rate space expressed as

$$\xi(\dot{\varepsilon}) = \frac{\partial \ln\left(\frac{m}{m+1}\right)}{\partial \ln \dot{\varepsilon}} + m < 0 \quad (20)$$

The deviation of the instability parameter $\xi(\dot{\varepsilon})$ with the strain rate and temperature constitutes an instability map that may be constructed on the power dissipation map to define the areas of flow instability. The deformation space, where $\xi(\dot{\varepsilon}) < 0$, is predicted as the regime for the manifestation of flow instabilities. Moreover, the deformation mechanisms related to specific domains/regimes were validated by microstructural characterization.

The evaluation of η and $\xi(\dot{\varepsilon})$ was carried out using the interpolation of cubic splines of log (σ) vs. log $\dot{\varepsilon}$ at each temperature, as described in our previous work [32]. The value of η was then calculated as a function of the strain rate and temperature (Eq. (19)) for a particular true strain. The calculated η values were used to construct 3D power dissipation and 2D iso-efficiency contour maps. In addition, an instability map was developed using the $\xi(\dot{\varepsilon})$ parameter, evaluated as a function of the strain rate and temperature (Eq. (20)) for a particular strain:

The 3D power dissipation efficiency maps constructed for the Ti–14Cr alloy at a true strain of 0.2, 0.4, and 0.6, encompassing the strain rate and temperature ranges are shown in Fig. 9(a, c, e), respectively. Similarly, the 3D plots of the instability maps of the corresponding conditions are represented in Fig. 9(b, d, f). Finally, the processing maps are

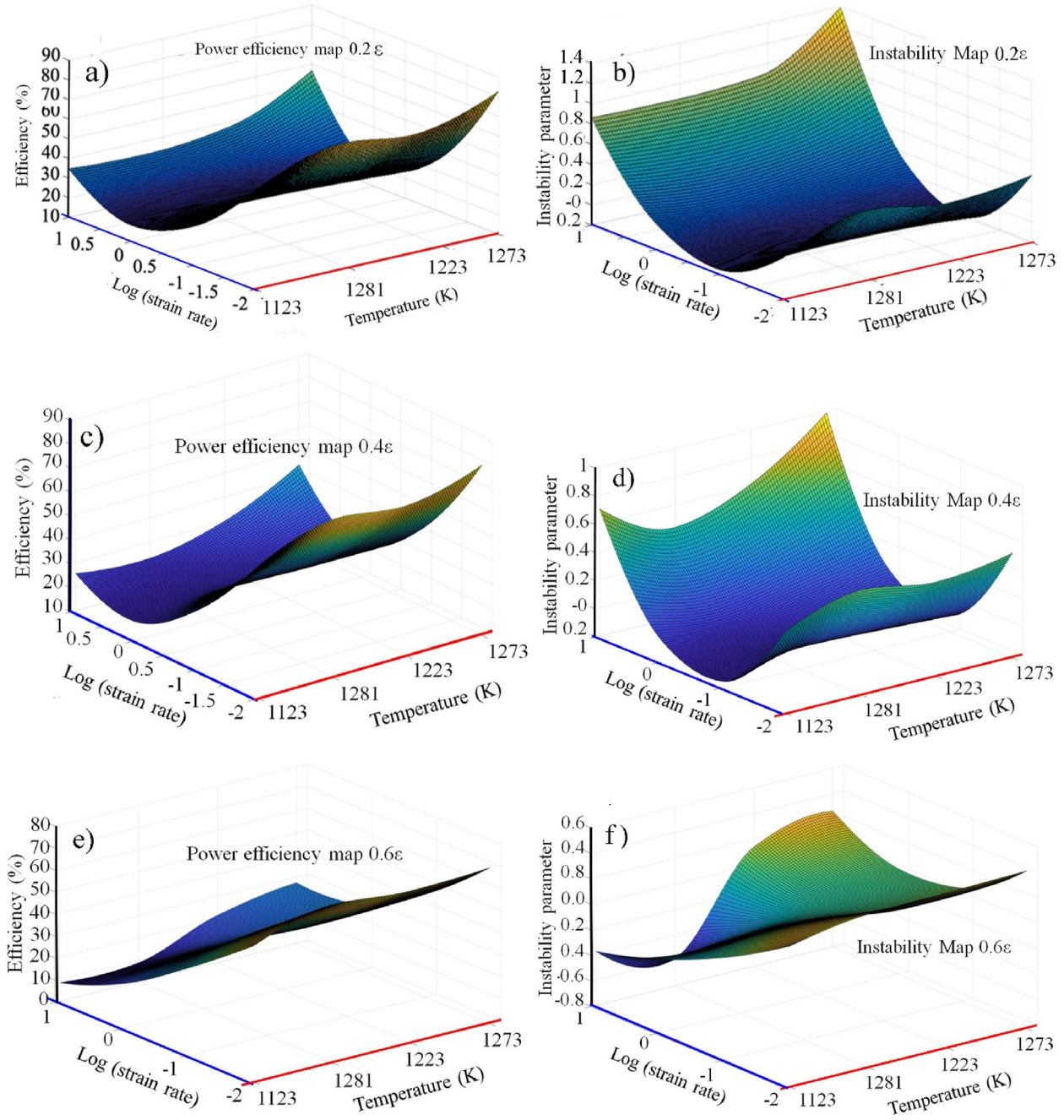

Fig. 9 – (a,c,e) 3D power dissipation iso-efficiency contour maps of Ti–14Cr alloy at $\varepsilon = 0.2$, 0.4 and 0.6 respectively, (b,d,f) 3D instability contour maps at $\varepsilon = 0.2$, 0.4 and 0.6 respectively.

constructed by superimposing the instability map on the power dissipation map and presented in Fig. 10(a,b,c).

Various deterministic domains and low-efficiency regimes of the processing maps were identified and interpreted in terms of the efficiencies of the power dissipation and possible microstructural mechanisms. Similarly, instability regimes were construed and substantiated regarding the instability manifestation. On the other hand, the power dissipation efficiency corresponding to the cracking process is generally high because the conversion of deformation energy into surface energy can be considered highly efficient. The peak power dissipation efficiencies of the DRX process are often nearly similar or closely located over a given strain range in the temperature–strain rate space, and they are relatively low-efficiency processes (<50%). In addition, the deformation at low strain rates and high temperatures exhibits higher elongation which is called superplastic deformations. Compared to the DRX process, the superplasticity occurs normally at lower strain rates that are several orders lower. The power dissipation efficiency is generally greater than 60% [60]. At low temperatures and high strain rates, adiabatic shear bands are likely to form with instabilities manifesting as

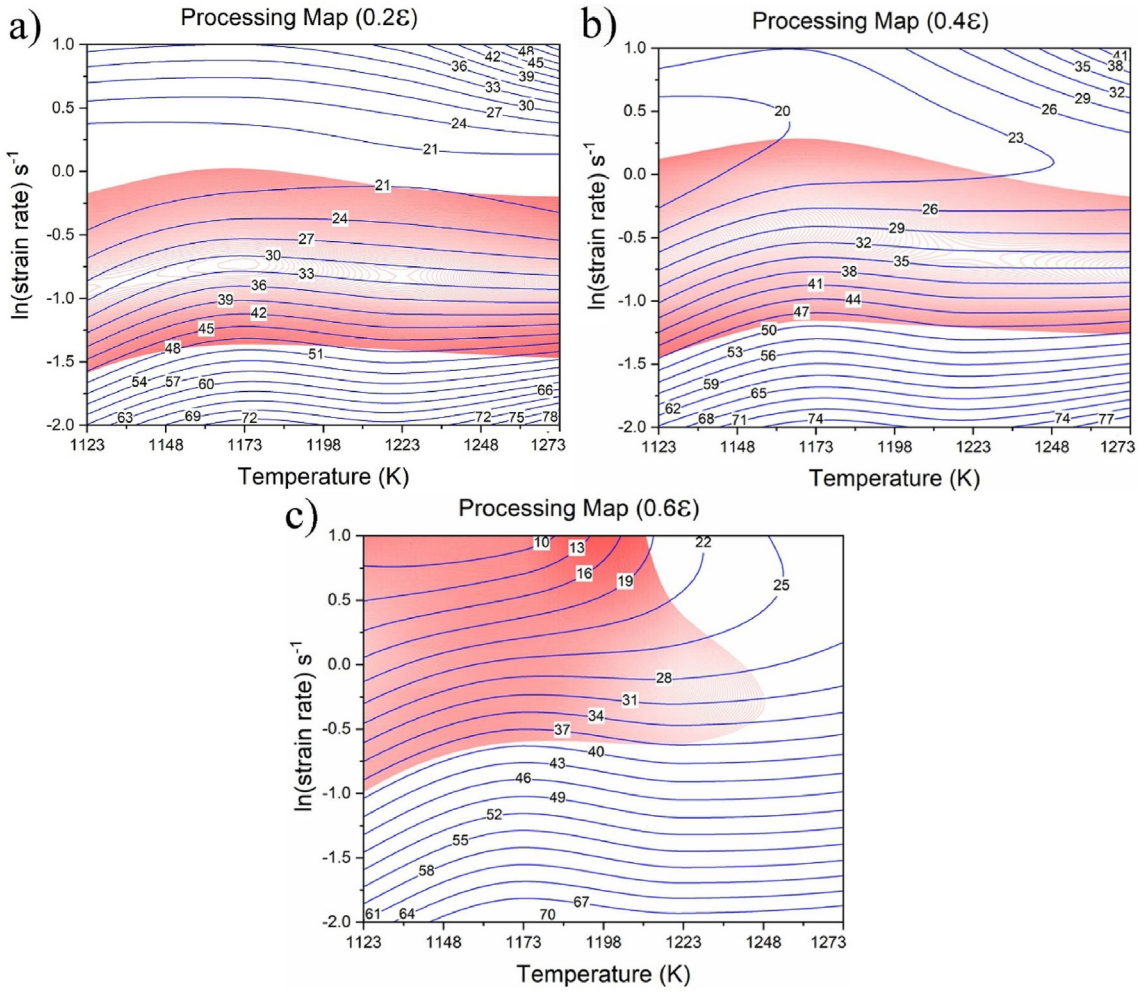

Fig. 10 – Processing maps of Ti–14Cr alloy at different strains: (a) $\varepsilon = 0.2$, (b) $\varepsilon = 0.4$, and (c) $\varepsilon = 0.6$. The region marked as red represents the instability regime.

intense bands, often associated with cracks or voids along these bands [75]. In contrast, at high temperatures and low strain rates, nucleation of wedge cracks is likely to occur at the grain boundaries (GBs), particularly at triple point junctions [76]. Therefore, the hot working in these regions of the processing map is 'unsafe'. In contrast, deterministic domains of DRX, superplasticity, and DRV are considered 'safe' processing domains. In the case of superplasticity, the larger strains can cause micropores along the GBs, therefore the processing with super plasticity is safer at smaller strains [60]. Fig. 10 presents the processing maps of the Ti–14Cr alloy constructed in the compression temperature range of 1123–1273 K and a strain rate range of 0.01–10 s^{-1} at strains of 0.4, 0.5, and 0.6. Each contour represents a constant efficiency. The red regions represent the instability regimes.

The processing maps constructed based on DMM corresponding to strains of 0.2, 0.4, and 0.6 show a high value of η at low strain rates (0.01–0.1 s^{-1}) that decreases as the strain rate increases. This observation may be correlated to diffusion control mechanisms (such as DRX and DRV), resulting in better workability. The processing map for the true strains of 0.2, 0.4, and 0.6 (Fig. 10(a, b, c), respectively) exhibits two domains: (i) in the temperature range of 1148–1273 K and strain rate range of 0.01–0.1 s^{-1} with a peak efficiency of ~70% occurring at approximately 1173 K and a strain rate of 0.01 s^{-1}, the high value of η may be attributed to continuous DRX/super plasticity mechanisms; (ii) another moderate iso-efficiency zone appeared in the high-temperature region ~1273 K at moderate/high strain rates (0.5–10 s^{-1}), which exhibited a peak efficiency of approximately 28% at ~1248 K and 0.5 s^{-1}, and this can be attributed to the dynamic recovery of the βTi structure.

Furthermore, it was noticed that the instability regimes are connected with high Z conditions, whereas deterministic domains supporting stable flow had relatively high η values occurring mostly in low Z conditions, where sufficient time is available for dislocation motion and deformation heating is avoided at low strain rates. In contrast, under high-Z conditions, adiabatic heat cannot be conducted in a short period time for high-strain-rate processes that lead to flow localisation [76]. Thus, the Ti–14Cr alloy possesses good intrinsic workability within the safe workable domains, where it can be

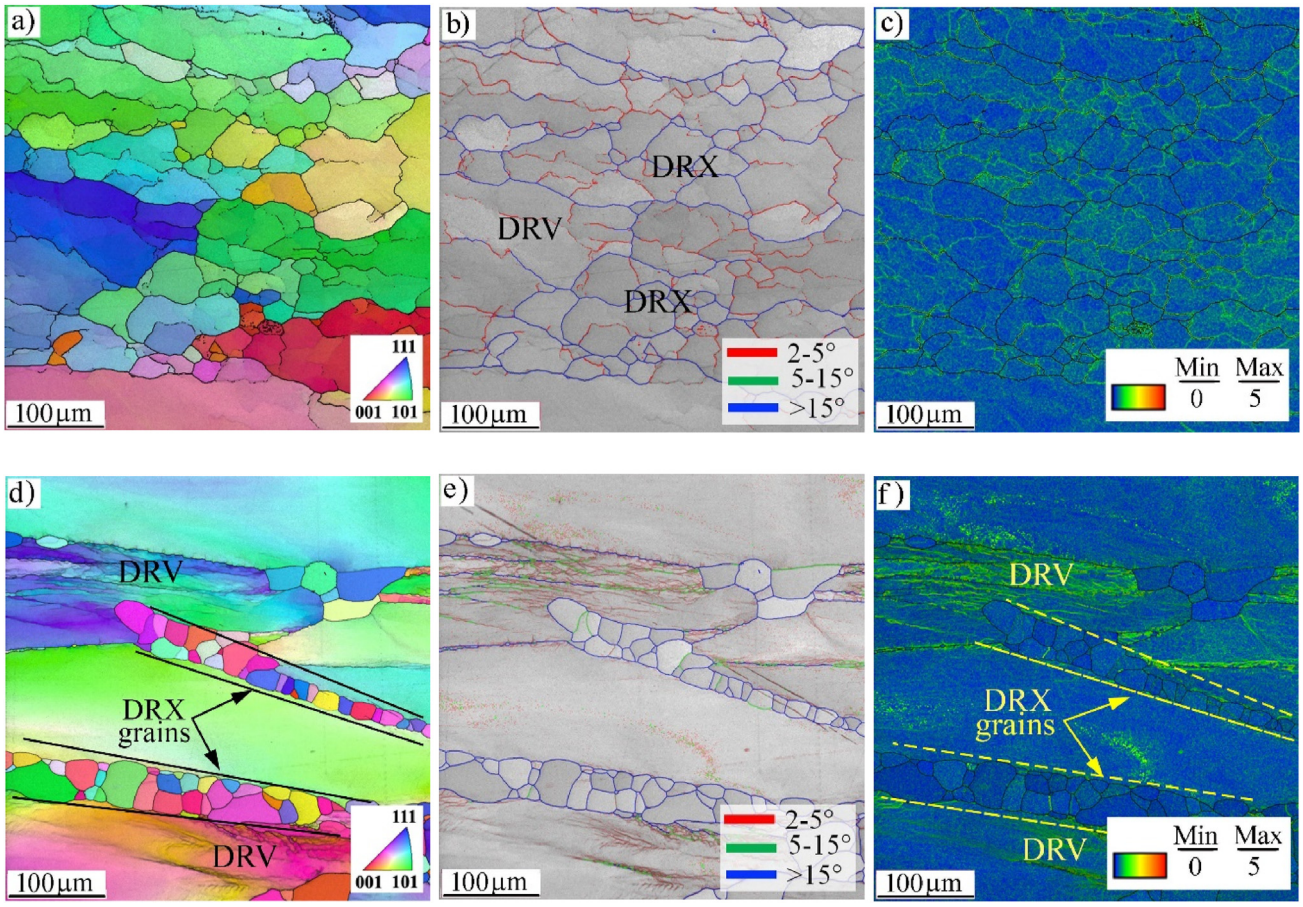

Fig. 11 – Microstructure of Ti–14Cr alloy deformed to 0.6 strain at 1273 K/0.01 s^{-1} (a, b, c) and 10 s^{-1} (d, e, f): (a, d) EBSD-boundary map, (b, e) misorientation map (low-angle boundaries in red color high angle grain boundaries in blue), and (c, f) related KAM maps.

safely processed with a reasonably high value of η, thus avoiding the instability regime.

3.6. *Microstructural development of the hot compressed samples*

The shape of the flow curves presented in Fig. 3 allows us to conclude that the DRX process had been initiated. Application of a true strain of 0.6 at the temperature of 1273 K with a strain rate equal to 0.01 s^{-1} allows the microstructure of nearly completely-recrystallized grains to be uniformly distributed in the matrix. However, few grains are dynamically recovered without subsequent recrystallization, as observed in (Fig. 11(a–c)). Low strain rates such as 0.01 s^{-1} are characterized owing to the material having sufficient time to initiate dynamic processes, and thus recrystallize the grains of the tested alloy. Increasing the strain rate of plastic deformation to 10 s^{-1} at temperature 1273 K reveals that dynamic recovery is the main mechanism that removes the effects of strain hardening during plastic deformation (Fig. 11(d–f)). Under such conditions, the microstructure of the alloy is composed of dynamically recovered grains elongated in the direction of plastic flow, with a recrystallized band of DDRX grains, as indicated by the black arrows in Fig. 11(d). The corresponding misorientation map, Fig. 11(e), confirms the new fine DRX grains via their HAGBs. The corresponding KAM map, Fig. 11(f) shows that the fine DRX grains have low KAM values (blue color) since, during recrystallization, the strain energy induced during deformation is consumed and the generated dislocations are absorbed to convert LAGBs into HAGB [77,78].

The strain rate 10 s^{-1} causes the deformation time to reduce below 0.1 s, which suggests that there is insufficient time to react and activate dynamic processes like recrystallization in the entire area of the deformed material, and thus the proportion of recrystallized grains is smaller in comparison to deformed samples with a lower value of strain rate. Increasing the strain rate from 0.01 to 10 s^{-1} and lowering the deformation temperature from 1273 to 1123 K reduced the participation of dynamically recrystallized grains (Figs. 11–13). For alloys deformed at 1123 K and 1173 K at a strain rate of 10 s^{-1} (Figs. 12(d) and 13(a)), the proportion of dynamically recrystallized grains is negligible, indicating that the main mechanism controlling strain hardening is dynamic recovery. The grains were elongated perpendicular to the direction of the compressive forces.

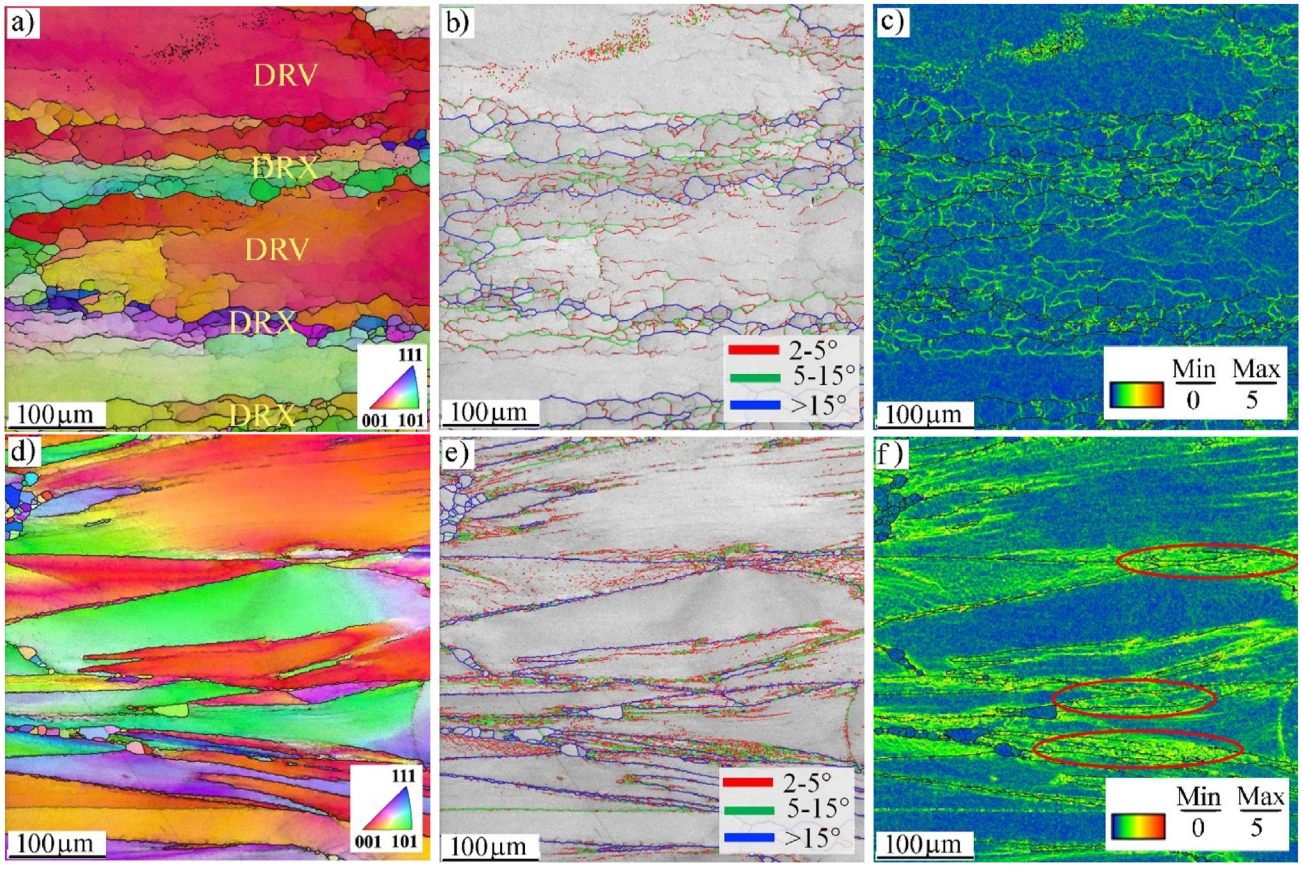

Fig. 12 – Microstructure of Ti–14Cr alloy deformed to 0.6 strain at 1173 K/0.01 s^{-1} (a, b, c) and 10 s^{-1} (d, e, f): (a, d) EBSD-boundary map, (b, e) misorientation map (low-angle boundaries in red color high angle grain boundaries in blue), and (c, f) related KAM maps.

This is consistent with the fact that DRV and CDRX are the predominant softening mechanisms in many β-Ti alloys. Hence, these mechanisms are critical for determining the deformation behavior of β-Ti alloys [40,71,79]. The Kernel Average Misorientation (KAM) map in Fig. 11(c) shows a uniform distribution at a high deformation temperature and a low strain rate. Low values of KAM existed in the center of the grain, and the maximum values of KAM were observed near the prior grain boundaries. Because the KAM map presents a medium misorientation for a certain point related to each of its direct neighbors, a high value of KAM concentration near the grain boundaries indicates a small misorientation toward the grain boundaries. Consequently, high values of KAM near the pre-existing grain boundaries and low values of KAM at the center of the deformed grain would suggest the occurrence of dynamic recovery followed by CDRX.

Fig. 12 shows the microstructure of the deformed material at 1173 K and different strain rates of 0.01 and 10 s^{-1}. It is observed that at a low strain rate of 0.01 s^{-1}, DRX grains are promoted near the prior grain boundaries, as marked in Fig. 12(a). The grain boundary map in Fig. 12(b) shows the dynamic recovery features. In addition, the uniform distribution of the KAM values, as shown in Fig. 12(c), indicates dynamic recovery control through this process instead of DRX. This is possible because of the high stacking fault energy of Ti–14Cr, which results in extensive and fast dynamic recovery. However, at a higher strain rate of 10 s^{-1}, no DRX grains are observed, as shown in Fig. 12(d). The misorientation map shows mainly LAGB with a low misorientation angle range of 2–5°, Fig. 12(e). Furthermore, the corresponding KAM map in Fig. 12(f) displayed high localized misorientation regions surrounding the deformed grain boundaries, i.e., high KAM values (green and yellow areas) highlighted by red ovals. This is associated with high residual dislocation density due to a high degree of strain suggesting the occurrence of DRV without DRX.

Fig. 13 shows the microstructures of the material tested at a higher deformation Z, i.e., a lower temperature of 1123 K. It is obvious that at a low strain rate of 0.01 s^{-1}, elongated grains with a large number of low-angle subgrain boundaries of 2–5° are observed inside the elongated grains, as shown in Fig. 13(b). Meanwhile, deformation bands (DBs) are promoted inside the grains as marked in Fig. 13(b). The KAM map showed a high localized misorientation at these boundaries, Fig. 13(c). It means that the level of DRV increases with decreasing the strain rate.

With increasing the strain rate to 10 s^{-1}, the microstructure is highly inhomogeneous, with an obvious flow-localized

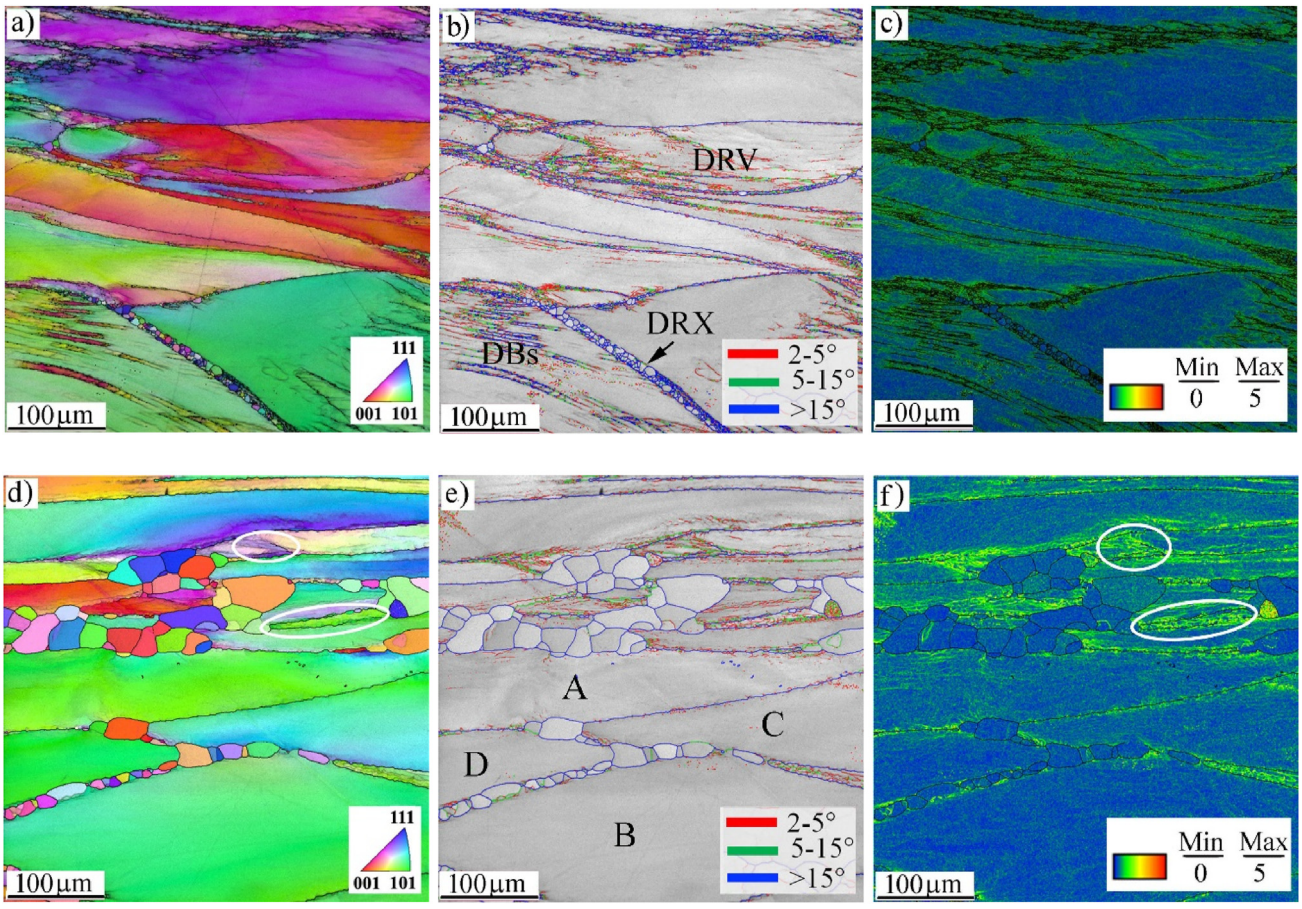

Fig. 13 – Microstructure of Ti–14Cr alloy deformed to 0.6 strain at 1123 K/0.01 s^{-1} (a, b, c) and 10 s^{-1} (d, e, f): (a, d) EBSD-boundary map, (b, e) misorientation map (low-angle boundaries in red color high angle grain boundaries in blue), and (c, f) related KAM maps.

band appearing along the shearing direction, as shown in Fig. 13(d). A striking feature of the corresponding misorientation map in Fig. 13(e) is the disappearance of subgrain boundaries of 2–5° in grains A, B, C, and D. This is attributed to the deformation strain that is accommodated at grain boundaries and DBs formed during hot deformation in compression testing. The corresponding KAM map reveals high localized misorientation, KAM values, at grain boundaries and deformation bands, as highlighted in Fig. 13(f).

4. Conclusions

1. The experimental data of the true stress–strain curves have been collected for a hot-rolled Ti–14Cr alloy through hot compression isothermal tests using a Gleeble simulator 3800, considering a range of temperatures (1123–1273 K) and strain rates (0.01–10 s^{-1}) to 0.6 true strain. In each condition, the flow stress increased with a reduction in the deformation temperature at a constant strain rate and with an increasing strain rate at a constant temperature.
2. The initial microstructure of Ti–14Cr consisted of equiaxed grains of the β-phase, indicating that 14 wt.% Cr stabilizes the β-phase at room temperature.
3. At the initial strains, the flow stress increased with increasing true strain regardless of the strain rate under all test conditions owing to work hardening.
4. At low strain rates (0.01–0.1 s^{-1}), the flow curves exhibited peak stress behavior and flow softening followed by a steady-state, implying the occurrence of DRX.
5. An Arrhenius-type constitutive equation was established for the true strain in the range of 0.1–0.6 which is valid for temperatures 1123–1273 K and strain rates 0.01–10 s^{-1}. The effect of the strain on the material constants is represented by sixth-order polynomial equations.
6. The validity of the Arrhenius-type model was checked via a comparison between the predicted and experimental flow stress. The average absolute relative error (AARE) and correlation coefficient (R) values were 9.66% and 0.9835, respectively, which confirmed that the constitutive model effectively depicted the hot deformation behavior and characteristics of Ti–14Cr alloy.
7. The processing map showed that adiabatic shear bands are expected to form at low temperatures and high strain rates, whereas the nucleation of wedge cracks is likely to develop at the grain boundary at high temperatures and low strain rates. Therefore, hot working in these regions of the processing map is not recommended, suggesting that

lower strain rates and temperatures are considered proper processing domains.

8. At lower strain rates, the flow curves show that the peak stress and flow softening behavior followed by a steady state were attained in the true flow stress curves, indicating the presence of DRX. The presence of DRX was confirmed by the microstructural investigation of the chosen samples.

Declaration of Competing Interest

The authors declare that they have no known competing financial interests or personal relationships that could have appeared to influence the work reported in this paper.

Acknowledgements

The authors express their gratitude to the Interreg Nord Program and the Regional Council of Lapland for funding this research through the InTeMP project, No. NYPS 20202486. Also, "Jane and Aatos Erkko Foundation" is appreciated for partly funding this study. Ebied expresses his gratitude to the Egyptian ministry of higher education and scientific research (missions sector) for funding his postdoctoral scholarship to produce the experimental material at Tohoku University, Japan.

REFERENCES

[1] United Nations, Department of Economic and Social Affairs, Population Division. World Population Ageing 2019 New York; 2020.

[2] Choi G, Lee K. Effect of cold rolling on the microstructural evolution of new β-typed Ti–6Mo–6V–5Cr–3Sn–2.5Zr alloys. Mater Char 2017;123:67–74. https://doi.org/10.1016/j.matchar.2016.11.007.

[3] Zhao X, Niinomi M, Nakai M, Hieda J, Ishimoto T, Nakano T. Optimization of Cr content of metastable β-type Ti–Cr alloys with changeable Young's modulus for spinal fixation applications. Acta Biomater 2012;8(6):2392–400. https://doi.org/10.1016/j.actbio.2012.02.010.

[4] Gouda MK, Salman SA, Ebied S. Improvement in the microhardness and corrosion behaviour of Ti-14Mn biomedical alloy by cold working. Mater Res Express 2022;9(1):015401. https://doi.org/10.1088/2053-1591/ac4b77.

[5] Santos PF, Niinomi M, Cho K, Nakai M, Liu H, Ohtsu N, et al. Microstructures, mechanical properties and cytotoxicity of low cost beta Ti–Mn alloys for biomedical applications. Acta Biomater 2015;26:366–76. https://doi.org/10.1016/j.actbio.2015.08.015.

[6] Ishimoto T, Hagihara K, Hisamoto K, Sun S-H, Nakano T. Crystallographic texture control of beta-type Ti–15Mo–5Zr–3Al alloy by selective laser melting for the development of novel implants with a biocompatible low Young's modulus. Scripta Mater 2017;132:34–8. https://doi.org/10.1016/j.scriptamat.2016.12.038.

[7] Zhao X, Niinomi M, Nakai M, Hieda J. Beta type Ti–Mo alloys with changeable Young's modulus for spinal fixation applications. Acta Biomater 2012;8(5):1990–7. https://doi.org/10.1016/j.actbio.2012.02.004.

[8] Lee W-S, Lin C-F, Chen T-H, Hwang H-H. Effects of strain rate and temperature on mechanical behaviour of Ti–15Mo–5Zr–3Al alloy. J Mech Behav Biomed Mater 2008;1(4):336–44. https://doi.org/10.1016/j.jmbbm.2008.01.002.

[9] Lee SH, Todai M, Tane M, Hagihara K, Nakajima H, Nakano T. Biocompatible low Young's modulus achieved by strong crystallographic elastic anisotropy in Ti–15Mo–5Zr–3Al alloy single crystal. J Mech Behav Biomed Mater 2012;14:48–54. https://doi.org/10.1016/j.jmbbm.2012.05.005.

[10] Verstraeten SV, Aimo L, Oteiza PI. Aluminium and lead: molecular mechanisms of brain toxicity. Arch Toxicol 2008;82(11):789–802. https://doi.org/10.1007/s00204-008-0345-3.

[11] Keegan GM, Learmonth ID, Case CP. Orthopaedic metals and their potential toxicity in the arthroplasty patient. J Bone Joint Sur Br 2007;89-B(5):567–73. https://doi.org/10.1302/0301-620X.89B5.18903.

[12] Gouda MK, Salman SA, Ebied S, Ashmawy AM, Gepreel MAH, Chiba A. Biocompatibility and corrosion resistance of low-cost Ti–14Mn–Zr alloys. J Mater Res 2021;36(24):4883–93. https://doi.org/10.1557/s43578-021-00441-w.

[13] Hao YL, Li SJ, Sun SY, Zheng CY, Yang R. Elastic deformation behaviour of Ti–24Nb–4Zr–7.9Sn for biomedical applications. Acta Biomater 2007;3(2):277–86. https://doi.org/10.1016/j.actbio.2006.11.002.

[14] Zhang T, Wei D, Lu E, Wang W, Wang K, Li X, et al. Microstructure evolution and deformation mechanism of α+β dual-phase Ti-xNb-yTa-2Zr alloys with high performance. J Mater Sci Technol 2022;131:68–81. https://doi.org/10.1016/j.jmst.2022.04.052.

[15] Xiao Ping'an, Hui Song Xuan, Wishes Lei Changming, Qin Baojun, li Ming, Ao Hui, et al. High temperature oxidation behaviors of Ti-Cr alloys with Laves phase TiCr2. Trans Nonferrous Metals Soc China 2002;12(2):200–3.

[16] Ho W-F, Cheng C-H, Chen W-K, Wu S-C, Lin H-C, Hsu H-C. Evaluation of low-fusing porcelain bonded to dental cast Ti–Zr alloys. J Alloys Compd 2009;471(1):185–9. https://doi.org/10.1016/j.jallcom.2008.03.040.

[17] Zhao XF, Niinomi M, Nakai M, Hieda J. Young's modulus changeable β-type binary Ti-Cr alloys for spinal fixation applications. Key Eng Mater 2012;508:117–23. https://doi.org/10.4028/www.scientific.net/KEM.508.117.

[18] Matthew J, Donachie J. Titanium: a technical guide. Materials Park, Ohio, USA: ASTM International; 2000. p. 381.

[19] Hanawa T, Asami K, Asaoka K. Repassivation of titanium and surface oxide film regenerated in simulated bioliquid. J Biomed Mater Res 1998;40(4):530–8. https://doi.org/10.1002/(SICI)1097-4636(19980615)40:4<530::AID-JBM3>3.0.CO;2-G.

[20] Ong JL, Lucas LC, Gn Raikar, Connatser R, Gregory JC. Spectroscopic characterization of passivated titanium in a physiologic solution. J Mater Sci Mater Med 1995;6(2):113–9. https://doi.org/10.1007/BF00120418.

[21] Hanawa T, Ota M. Characterization of surface film formed on titanium in electrolyte using XPS. Appl Surf Sci 1992;55(4):269–76. https://doi.org/10.1016/0169-4332(92)90178-Z.

[22] Hanada S, Izumi O. Deformation behaviour of retained β phase inβ-eutectoid Ti-Cr alloys. J Mater Sci 1986;21(12):4131–9. https://doi.org/10.1007/BF01106518.

[23] Ho W-F, Chiang T-Y, Wu S-C, Hsu H-C. Mechanical properties and deformation behavior of cast binary Ti–Cr alloys. J Alloys Compd 2009;468(1):533–8. https://doi.org/10.1016/j.jallcom.2008.01.046.

[24] Ebied S, Hamada A, Borek W, Gepreel M, Chiba A. High-temperature deformation behavior and microstructural characterization of high-Mn bearing titanium-based alloy.

Mater Char 2018;139:176–85. https://doi.org/10.1016/j.matchar.2018.03.004.
[25] Jing L, Fu RD, Wang YP, Qiu L, Yan B. Discontinuous yielding behavior and microstructure evolution during hot deformation of TC11 alloy. Mater Sci Eng, A 2017;704:434–9. https://doi.org/10.1016/j.msea.2017.08.048.
[26] Jonas JJ, Aranas C, Fall A, Jahazi M. Transformation softening in three titanium alloys. Mater Des 2017;113:305–10. https://doi.org/10.1016/j.matdes.2016.10.039.
[27] Zhao QY, Yang F, Torrens R, Bolzoni L. Evaluation of the hot workability and deformation mechanisms for a metastable beta titanium alloy prepared from powder. Mater Char 2019;149:226–38. https://doi.org/10.1016/j.matchar.2019.01.031.
[28] Fujita N, Ishikawa N, Roters F, Tasan CC, Raabe D. Experimental–numerical study on strain and stress partitioning in bainitic steels with martensite–austenite constituents. Int J Plast 2018;104:39–53. https://doi.org/10.1016/j.ijplas.2018.01.012.
[29] Kestens LAI, Pirgazi H. Texture formation in metal alloys with cubic crystal structures. Mater Sci Technol 2016;32(13):1303–15. https://doi.org/10.1080/02670836.2016.1231746.
[30] Khosravifard A, Hamada AS, Moshksar MM, Ebrahimi R, Porter DA, Karjalainen LP. High temperature deformation behavior of two as-cast high-manganese TWIP steels. Mater Sci Eng, A 2013;582:15–21. https://doi.org/10.1016/j.msea.2013.06.014.
[31] Hamada A, Khosravifard A, Porter D, Pentti Karjalainen L. Physically based modeling and characterization of hot deformation behavior of twinning-induced plasticity steels bearing vanadium and niobium. Mater Sci Eng, A 2017;703:85–96. https://doi.org/10.1016/j.msea.2017.07.038.
[32] Patnamsetty M, Somani MC, Ghosh S, Ahmed S, Peura P. Processing map for controlling microstructure and unraveling various deformation mechanisms during hot working of CoCrFeMnNi high entropy alloy. Mater Sci Eng, A 2020;793:139840. https://doi.org/10.1016/j.msea.2020.139840.
[33] Dong F, Yuan Y, Li W, Zhang Y, Liaw PK, Yuan X, et al. Hot deformation behavior and processing maps of an equiatomic MoNbHfZrTi refractory high entropy alloy. Intermetallics 2020;126:106921. https://doi.org/10.1016/j.intermet.2020.106921.
[34] Jeong HT, Park HK, Kim WJ. Hot deformation behavior and processing map of a Sn0.5CoCrFeMnNi high entropy alloy with dual phases. Mater Sci Eng, A 2021;801:140394. https://doi.org/10.1016/j.msea.2020.140394.
[35] Peters M, Hemptenmacher J, Kumpfert J, Leyens C. Structure and properties of titanium and titanium alloys. In: Leyens Christoph, Peters M, editors. Titanium and titanium alloys: fundamentals and applications. Wiley-VCH Verlag GmbH & Co. KGaA; 2003. p. 1–36.
[36] Lai MJ, Li T, Raabe D. ω phase acts as a switch between dislocation channeling and joint twinning- and transformation-induced plasticity in a metastable β titanium alloy. Acta Mater 2018;151:67–77. https://doi.org/10.1016/j.actamat.2018.03.053.
[37] Łukaszek-Sołek A, Krawczyk J. The analysis of the hot deformation behaviour of the Ti–3Al–8V–6Cr–4Zr–4Mo alloy, using processing maps, a map of microstructure and of hardness. Mater Des 2015;65:165–73. https://doi.org/10.1016/j.matdes.2014.09.023.
[38] Gouda MK, Gepreel MAH, Yamanaka K, Bian H, Nakamura K, Chiba A. Cold-workability and microstructure change with β-phase stability in high-strength Ti-Mn binary alloys. J Occup Med 2019;71(10):3590–9. https://doi.org/10.1007/s11837-019-03690-7.
[39] Zheng Y, Williams REA, Wang D, Shi R, Nag S, Kami P, et al. Role of ω phase in the formation of extremely refined intragranular α precipitates in metastable β-titanium alloys. Acta Mater 2016;103:850–8. https://doi.org/10.1016/j.actamat.2015.11.020.
[40] Balasubrahmanyam VV, Prasad YVRK. Deformation behaviour of beta titanium alloy Ti–10V–4.5Fe–1.5Al in hot upset forging. Mater Sci Eng, A 2002;336(1):150–8. https://doi.org/10.1016/S0921-5093(01)01982-7.
[41] Abbasi SM, Morakkabati M, Sheikhali AH, Momeni A. Hot deformation behavior of beta titanium Ti-13V-11Cr-3Al alloy. Metall Mater Trans 2014;45(11):5201–11. https://doi.org/10.1007/s11661-014-2464-1.
[42] Xu X, Dong L-m, Ba H-b, Zhang Z-q, Yang R. Hot deformation behavior and microstructural evolution of beta C titanium alloy in β phase field. Trans Nonferrous Metals Soc China 2016;26(11):2874–82. https://doi.org/10.1016/S1003-6326(16)64416-3.
[43] Kou H, Chen Y, Tang B, Cui Y, Sun F, Li J, et al. An experimental study on the mechanism of texture evolution during hot-rolling process in a β titanium alloy. J Alloys Compd 2014;603:23–7. https://doi.org/10.1016/j.jallcom.2014.03.070.
[44] Zhang C, Lü Z, Wu J, Guo C, Zhang S, Han J, et al. Hot deformation behavior and microstructure evolution of a new near β titanium alloy reinforced with trace TiCp. Adv Eng Mater 2019;21(2):1800747. https://doi.org/10.1002/adem.201800747.
[45] Gao PF, Guo J, Zhan M, Lei ZN, Fu MW. Microstructure and damage based constitutive modelling of hot deformation of titanium alloys. J Alloys Compd 2020;831:154851. https://doi.org/10.1016/j.jallcom.2020.154851.
[46] Fan XG, Zhang Y, Gao PF, Lei ZN, Zhan M. Deformation behavior and microstructure evolution during hot working of a coarse-grained Ti-5Al-5Mo-5V-3Cr-1Zr titanium alloy in beta phase field. Mater Sci Eng, A 2017;694:24–32. https://doi.org/10.1016/j.msea.2017.03.095.
[47] Matsumoto H, Kitamura M, Li Y, Koizumi Y, Chiba A. Hot forging characteristic of Ti–5Al–5V–5Mo–3Cr alloy with single metastable β microstructure. Mater Sci Eng, A 2014;611:337–44. https://doi.org/10.1016/j.msea.2014.06.006.
[48] Liu SF, Li MQ, Luo J, Yang Z. Deformation behavior in the isothermal compression of Ti–5Al–5Mo–5V–1Cr–1Fe alloy. Mater Sci Eng, A 2014;589:15–22. https://doi.org/10.1016/j.msea.2013.09.066.
[49] Sheikhali AH, Morakkabati M, Abbasi SM, Rezaei A. Superplasticity of coarse-grained Ti-13V-11Cr-3Al alloy. Int J Mater Res 2013;104(11):1122–7. https://doi.org/10.3139/146.110965.
[50] Fan JK, Kou HC, Lai MJ, Tang B, Chang H, Li JS. Hot deformation mechanism and microstructure evolution of a new near β titanium alloy. Mater Sci Eng, A 2013;584:121–32. https://doi.org/10.1016/j.msea.2013.07.019.
[51] Li C, Huang L, Zhao M, Guo S, Li J. Hot deformation behavior and mechanism of a new metastable β titanium alloy Ti–6Cr–5Mo–5V–4Al in single phase region. Mater Sci Eng, A 2021;814:141231. https://doi.org/10.1016/j.msea.2021.141231.
[52] Kolli RP, Joost WJ, Ankem S. Phase stability and stress-induced transformations in beta titanium alloys. J Occup Med 2015;67(6):1273–80. https://doi.org/10.1007/s11837-015-1411-y.
[53] Ebied S, Hamada A, Gadelhaq MHA, Yamanaka K, Bian H, Cui Y, et al. Study on hot deformation behavior of beta Ti-

17Mo alloy for biomedical applications. J Occup Med 2022;74(2):494–505. https://doi.org/10.1007/s11837-021-05060-8.
[54] Ebied SM, Gepreel MA-H, Hamada A. Microstructural evolution of two binary β-titanium alloys during cold deformation. IOP Conf Ser Mater Sci Eng 2017;201:012047. https://doi.org/10.1088/1757-899X/201/1/012047.
[55] Yabe H, Kuji T. Mechanically driven b.c.c. TiCr alloy and its hydrogen solubility. J Alloys Compd 2005;404–406:533–6. https://doi.org/10.1016/j.jallcom.2005.01.116.
[56] Ghosh S, Kömi J, Mula S. Flow stress characteristics and design of innovative 3-steps multiphase control thermomechanical processing to produce ultrafine grained bulk steels. Mater Des 2020;186:108297. https://doi.org/10.1016/j.matdes.2019.108297.
[57] Prasad YVRK, Ravichandran N. Effect of stacking fault energy on the dynamic recrystallization during hot working of FCC metals: a study using processing maps. Bull Mater Sci 1991;14(5):1241–8. https://doi.org/10.1007/BF02744618.
[58] Wang F, Li Y, Xie G, Wakoh K, Yamanaka K, Koizumi Y, et al. Investigation on hot deformation behavior of nanoscale TiC-strengthened Cu alloys fabricated by mechanical milling. Mater Sci Eng, A 2016;668:1–12. https://doi.org/10.1016/j.msea.2016.05.042.
[59] Ghosh S, Patnamsetty M, Somani MC, Peura P. Characteristics of dynamic softening during high temperature deformation of CoCrFeMnNi high-entropy alloy and its correlation with the evolving microstructure and micro-texture. J Mater Res Technol 2021;15:6608–23. https://doi.org/10.1016/j.jmrt.2021.11.089.
[60] Prasad Y, Rao KP, Sasidhar S. Hot working guide: a compendium of processing maps. ASM international; 2015. p. 638.
[61] Hamada A, Juuti T, Khosravifard A, Kisko A, Karjalainen P, Porter D, et al. Effect of silicon on the hot deformation behavior of microalloyed TWIP-type stainless steels. Mater Des 2018;154:117–29. https://doi.org/10.1016/j.matdes.2018.05.029.
[62] Sellars CM, McTegart WJ. On the mechanism of hot deformation. Acta Metall 1966;14(9):1136–8. https://doi.org/10.1016/0001-6160(66)90207-0.
[63] McQueen HJ, Ryan ND. Constitutive analysis in hot working. Mater Sci Eng, A 2002;322(1):43–63. https://doi.org/10.1016/S0921-5093(01)01117-0.
[64] Ghosh S, Somani MC, Setman D, Mula S. Hot deformation characteristic and strain dependent constitutive flow stress modelling of Ti + Nb stabilized interstitial free steel. Met Mater Int 2021;27(8):2481–98. https://doi.org/10.1007/s12540-020-00827-1.
[65] Ghosh S, Somani MC, Setman D, Mula S. Elucidation of deformation mechanisms and construction of processing maps for a Ti+Nb stabilized IF steel. Mater Sci Eng, A 2020;790:139648. https://doi.org/10.1016/j.msea.2020.139648.
[66] Wan P, Zou H, Wang K, Zhao Z. Hot deformation characterization of Ti–Nb alloy based on GA-LSSVM and 3D processing map. J Mater Res Technol 2021;13:1083–97. https://doi.org/10.1016/j.jmrt.2021.05.019.
[67] Patnamsetty M, Saastamoinen A, Somani MC, Peura P. Constitutive modelling of hot deformation behaviour of a CoCrFeMnNi high-entropy alloy. Sci Technol Adv Mater 2020;21(1):43–55. https://doi.org/10.1080/14686996.2020.1714476.
[68] Lu C, Shi J, Wang J. Physically based constitutive modeling for Ti17 alloy with original basketweave microstructure in β forging: a comparison of three approaches. Mater Char 2021;181:111455. https://doi.org/10.1016/j.matchar.2021.111455.
[69] Gao S, Sang Y, Li Q, Sun Y, Wu Y, Wang H. Constitutive modeling and microstructure research on the deformation mechanism of Ti-6Al-4V alloy under hot forming condition. J Alloys Compd 2022;892:162128. https://doi.org/10.1016/j.jallcom.2021.162128.
[70] Chenwei L, Hui X, Xiaonan M, Pengsheng Z, Zhimin H. High temperature deformation of TC18 titanium alloy. Rare Met Mater Eng 2017;46(2):326–32. https://doi.org/10.1016/S1875-5372(17)30089-9.
[71] Sun Y, Zeng WD, Zhao YQ, Zhang XM, Shu Y, Zhou YG. Research on the hot deformation behavior of Ti40 alloy using processing map. Mater Sci Eng, A 2011;528(3):1205–11. https://doi.org/10.1016/j.msea.2010.10.019.
[72] Zhang Z, Fan J, Tang B, Kou H, Wang J, Chen Z, et al. Microstructure/texture evolution maps to optimize hot deformation process of near-α titanium alloy. Prog Nat Sci: Mater Int 2020;30(1):86–93. https://doi.org/10.1016/j.pnsc.2020.01.004.
[73] Prasad YVRK, Gegel HL, Doraivelu SM, Malas JC, Morgan JT, Lark KA, et al. Modeling of dynamic material behavior in hot deformation: forging of Ti-6242. Metall Trans A 1984;15(10):1883–92. https://doi.org/10.1007/BF02664902.
[74] Ziegler H, Becker E, Budiansky B, Lauwerier HA, Koiter T. An introduction to thermodynamics. 2nd ed. North-Holland Publishing Company; 1983.
[75] Liu C, Guan H, Tai Q, Yuan F, Han F, Gu H, et al. Microstructure, texture and mechanical studies of an inconspicuous shear band formed during hot compression of Ti-6Al-4V alloy. Mater Sci Eng, A 2017;698:18–26. https://doi.org/10.1016/j.msea.2017.05.041.
[76] Somani MC, Rao ESB, Birla NC, Bhatia ML, Singh V, Prasad YVRK. Processing map for controlling microstructure in hot working of hot isostatically pressed powder metallurgy NIMONIC AP-1 superalloy. Metall Trans A 1992;23(10):2849–57. https://doi.org/10.1007/BF02651762.
[77] Zhao T, Hu Y, He B, Zhang C, Zheng T, Pan F. Effect of manganese on microstructure and properties of Mg-2Gd magnesium alloy. Mater Sci Eng, A 2019;765:138292. https://doi.org/10.1016/j.msea.2019.138292.
[78] Li Z-J, Wang J-G, Yan R-F, Chen Z-Y, Ni T-Y, Dong Z-Q, et al. Effect of Ce addition on hot deformation behavior and microstructure evolution of AZ80 magnesium alloy. J Mater Res Technol 2022;16:1339–52. https://doi.org/10.1016/j.jmrt.2021.12.083.
[79] Philippart I, Rack HJ. High temperature dynamic yielding in metastable Ti–6.8Mo–4.5F–1.5Al. Mater Sci Eng, A 1998;243(1):196–200. https://doi.org/10.1016/S0921-5093(97)00800-9.